Enhanced Adsorption of Anionic Polymer on Montmorillonite by Divalent Cations and the Effect of Salinity

Wenyuan Sun[†], Hongbo Zeng[‡] and Tian Tang*[,†]

[†]Department of Mechanical Engineering and [‡]Department of Chemical and Materials Engineering, University of Alberta, Edmonton, Alberta T6G 1H9, Canada

* Corresponding author, email: tian.tang@ualberta.ca, phone: +1-780-492-5467.

Abstract

Adsorption of polymers from an aqueous solution onto clay minerals is of great interest to many applications such as water purification and soil conditioning. Molecular dynamics simulations were performed to study the adsorption of anionic polyacrylamide (APAM) on anionic montmorillonite, in an aqueous solution containing monovalent or divalent salts. Compared with monovalent salts (NaCl), the enhancement of APAM adsorption brought by divalent salts ($CaCl_2$) was significant, which could not be explained by the Poisson-Boltzmann theory alone. Each solvated Ca^{2+} was coordinated by 4-6 water oxygens in its first coordination shell. One to two of these water molecules were displaced when APAM formed a complex with Ca^{2+}. Ca^{2+} ions in the adsorbed Ca^{2+}-APAM complexes did not serve as bridges sandwiched between APAM and Mt; instead the complexes carried residual positive charge and were subsequently attracted to montmorillonite. The number of adsorbed Ca^{2+}-APAM complexes changed with salinity in a non-monotonic manner, due to the modulation of apparent charges of montmorillonite and APAM by Ca^{2+}. Increasing adsorption of Ca^{2+}-APAM complexes also promoted APAM adsorption through direct hydrogen bonding with montmorillonite. The findings provided new molecular insights into the long-standing debates on the role of divalent ions in promoting polymer adsorption on like-charged solid surfaces.

Keywords: anionic polyacrylamide; montmorillonite; polymer adsorption; divalent salt

1. Introduction

Polymer adsorption at solid-liquid interfaces is ubiquitous in many industrial applications. For example, the adsorption of supramolecular complexes composed of polymers (e.g., poly(diallyldimethylammonium chloride), PDADMAC) on keratinic substrate (hair) is of great interest in the design of conditioner cosmetic formulations[1]. Intercalation of polymer chains (e.g., chitosan) into clay mineral layers in aqueous environment is a widely used method in the fabrication of nanocomposites[2]. In many industrially produced waters, polymeric wastes such as polymeric dyes can be collected via their adsorption onto synthesized adsorbents[3,4], and likewise waste suspensions of fine solids can be treated by polymer flocculants (e.g., polyacrylamide)[5].

In particular, interaction between solid particles in colloidal systems may be modulated by controlled polymer adsorption onto the solid particles. For example, water-soluble cellulose polymers were widely used to regulate the interactions between drug particles in pharmaceutical formulations, promoting their stabilities. Drug particles such as ibuprofen became well dispersed in the suspension due to the steric effect produced by the adsorbed polymer layers[6]. Thickness as well as the composition of the adsorbed layer were among the most important factors affecting the strength of the steric interaction. On the other hand, polymers could also promote aggregation of solid particles and solid-liquid phase separation in many colloidal systems[7,8]. Via adsorption, the polymers could provide hydrogen bonding (H-bonding) sites or charge patches on the surfaces of solid particles, enabling inter-particle attraction. Understanding the behaviors of polymer molecules as they adsorb on solid surfaces is thus of great importance to modulating the properties of colloidal dispersions.

In an aqueous medium, interaction between polymer molecules and solid particles is largely affected by the solution chemistry[9,10]. Certain polymers and solids can become charged from the dissociation and ionization of functional groups into the solution. The charge properties (e.g., charge density, charge distribution or pattern) are sensitive to the constituents of the solution, such as salt ions. The effects of salt ions on solid-polymer interactions have been extensively investigated because of the wide existence of salts in many systems such as cosmetics, wastewater, and drugs[11,12]. Ions have been shown to markedly improve polymer adsorption, especially when the polymer and the solid are like-charged. For example, Ji et al.[13] compared the settling rate of negatively charged solid particles in saline water and freshwater, both treated by Magnafloc 1011 (MF, an anionic copolymer of polyacrylamide and sodium acrylate). The

settling relied on MF adsorbing on the fine particles and subsequently bridging them into larger aggregates/flocs. It was shown that the solids settled faster in saline water. The observation was attributed to the compressed electrical double layer caused by high salinity, which led to enhanced polymer adsorption and suppressed electrostatic repulsion among the particles. Zeta potential measurements confirmed such a hypothesis, which showed a less negative surface charge on the solid particles in saline water than in freshwater.

The valence of ions has been shown to have a pronounced effect on the adsorption of polymers on like-charged surfaces in aqueous media[14–19]. Deng et al.[14] studied the impact of cations (Na^+, K^+, Mg^{2+}, Ca^{2+}) on the adsorption of anionic polyacrylamide (APAM) on anionic smectite, using Fourier transform infrared spectroscopy (FTIR) and X-ray diffraction. By comparing the IR-band positions among the APAM-smectite complexes containing different cations, it was deduced that APAM bound more strongly to smectites in solutions containing divalent cations (Mg^{2+}, Ca^{2+}) than those containing monovalent cations (Na^+, K^+). The adsorption of APAM was believed to be mainly driven by the ion-dipole interactions, which was stronger between the divalent cations and the carbonyl dipole of APAM. Vermöhlen et al.[15] observed a higher adsorption isotherm of polyelectrolytes (polyacrylic acid, polymethacrylic acid, and humic acid) onto oxide surfaces (gibbsite, goethite, and alumina) in 0.0033 M $CaCl_2$ solution, compared with 0.01 M NaCl solution. It was proposed that divalent cations served as bridges between the negatively charged polyelectrolytes and adsorbent, in addition to suppressing the electrostatic repulsion between them. Similar observation was made by Braganca et al.[16], who prepared nanocomposites from montmorillonite (Mt) and styrene-acrylic latex in an aqueous medium, both possessing negative charges. When varying the cation valence, better adhesion between Mt and styrene-acrylic latex was found in the presence of Ca^{2+} than Na^+, which was attributed to the formation of Ca^{2+} bridges. However, an opposite observation was reported by Ait-Akbour et al.[17], who measured the adsorption isotherm of PCP (negatively charged polycarboxylate poly(ethylene glycol) ester) in the interlayer space of Mt containing different cations. Mg^{2+}, Ca^{2+} and Na^+ were considered, and the systems were referred to as Mg-Mt, Ca-Mt, and Na-Mt respectively. Decreased PCP adsorption was found in the interlayer space of Mg-Mt and Ca-Mt compared with Na-Mt. It was postulated that cations were coordinated to water molecules in their solvation. PCP adsorbed to the Mt interlayers via the cations, by displacing the water molecules in the coordination shell of the cations. The displacement of water was argued

to be more difficult for Ca^{2+}/Mg^{2+}, based on their more negative solvation energy (-553.6 kJ mol^{-1}/-454.8 kJ mol^{-1}) than Na^{+} (-261.9 kJ mol^{-1}). Other roles of the valence were also proposed. For instance, Santos et al.[18] and Wang et al.[19] performed theoretic calculations that predicted multivalent cations to promote the adsorption of anionic polyelectrolyte on a like-charged planar surface. They proposed that the enhancement was due to the stronger electrostatic correlation effects brought by the multivalent cations, which could cause the planar surface to be reversely charged.

The effects of multivalent ions on polymer adsorption are also tied to the salinity of the solution. The adsorption isotherm of polyelectrolytes on oxide sufaces in Vermöhlen et al.[15] increased with $CaCl_2$ concentration. This result was explained by the stronger screening of the negative charges on both the solid surfaces and the polymers at higher salt concentration. However, a contradictory conclusion was drawn by Peng et al.[9], who measured the height of clear supernatant of kaolinite suspensions treated by APAM, with 0 mol/dm^3, 0.0005 mol/dm^3, and 0.001 mol/dm^3 of $CaCl_2$. The hydroxyl groups on the surface of kaolinite particles could enable APAM adsorption through H-bonding, followed by the settling of kaolinite particles bridged by the polymer chains. The height of clear supernatant in the suspension would thus increase with solid settling. It was reported that the height of clear supernatant decreased with $CaCl_2$ concentration, suggesting less APAM adsorption at higher salinity. The authors held the view that the presence of Ca^{2+} triggered precipitation of calcium hydroxyl on the active sites of kaolinite, preventing the formation of H-bonds between kaolinite and APAM.

In summary, while the adsorption of anionic polymers on like-charged solid surfaces was generally shown to be promoted by salts, various mechanisms have been proposed from different experimental observations, some seemingly conflicting. Ambiguities on the effect of valence and its interplay with salinity are better addressed if a molecular-level picture can be painted providing direct visualization of the interactions between polymers and solid surfaces. Motivated by this, molecular dynamics (MD) simulation has been employed in this work to study the adsorption of a representative polyanion on an anionic model surface. The objectives were two-fold: to reveal the role of the valence of ions, by simulating both NaCl and $CaCl_2$ solutions; and to address the effect of salinity, by applying a series of different salt concentrations.

2. Simulation methods

2.1 Models & Systems

APAM was chosen as the representative polyanion, which has been popularly used to enhance solid particle aggregation in colloidal suspensions[9,13,20,21]. The simulated APAM model had a molecular weight (MW) of 641 g/mol ($C_{27}H_{44}N_6O_{12}$, Figure 1a), with every third amide group substituted by a carboxylate group, resulting in a charge of -3. All carboxylate groups of APAM were deprotonated to represent a neutral to slightly alkaline pH condition[22,23], which is typical in polymer-clay systems[24]. The solid surface was represented by a negatively charged molecular model of Mt, a common clay mineral[12,25–27]. Mt is an aluminosilicate usually referred to as 2:1 or TOT layer: it is composed of a central sheet with octahedrally coordinated Al atoms, sandwiched between two other sheets with tetrahedrally coordinated Si atoms[28]. A 2 × 2 × 1 supercell was first developed by closely stacking the neutral unit cells in three dimensions, followed by isomorphically substituting three random Al atoms with Mg. The substitution of +3 charged Al atoms by +2 charged Mg atoms in the central octahedral sheet resulted in a local charge deficiency, and the net charge of this supercell became -3. Then the 2 × 2 × 1 cell with a permanent layer charge was expanded to a 16 × 10 × 1 supercell, as shown in Figure 1b, carrying a negative charge of -120.

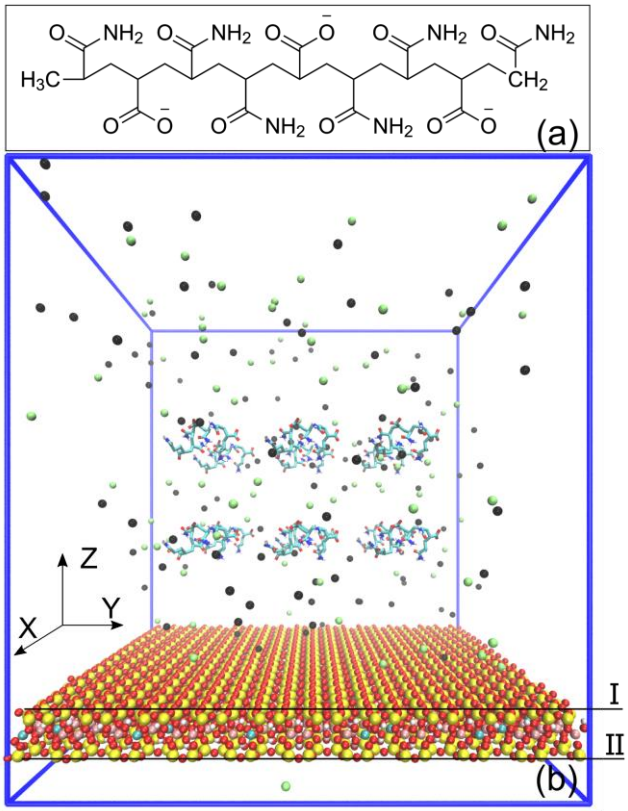

Figure 1 (a) Molecular structure of APAM and (b) initial configuration of system Ca-0.1. In (b), Mt is represented by balls, and two basal surfaces are marked by I and II respectively. Color scheme for atoms in Mt: Si (yellow), Al (pink), Mg (cyan), O (red), and H (white). APAM is represented by licorice with C (green) and N (blue). The solvent, water, is removed for clarity, whereas ions are shown as Ca^{2+} (black) and Cl^- (lime).

To investigate the adsorption of APAM on Mt in presence of salts, a series of 7 simulations, divided into two sets, were performed (Table 1). The first set investigated the effect of valence of cations, where 0.5 M NaCl was solvated into system Na-0.5 in addition to the Na^+ used to neutralize the negative charges of Mt, and similarly 0.5 M $CaCl_2$ was introduced in system Ca-0.5 in addition to the neutralizing Ca^{2+}. Systems containing only the neutralizing ions were simulated for comparison, namely systems Na-0 and Ca-0. The second set of simulations were run to study APAM adsorption in divalent salt solutions with different concentrations. Three additional systems were simulated, Ca-0.05, Ca-0.1 and Ca-0.3, corresponding to $CaCl_2$ concentration of 0.05 M, 0.1 M and 0.3 M. In each simulation, the supercell of Mt was placed at the bottom of a simulation box with dimension of 8.30 × 8.95 × 10.0 nm^3. A total of 12 APAM molecules were then introduced above the Mt surface in a 2 × 3 × 2 array, followed by solvation

of the system with water and an appropriate amount of salt (Table 1). The initial configuration for Mt and APAM was the same for all systems and is represented by Figure 1b.

Table 1 Simulated Systems

system name	neutralizing ions	additional salt
Na-0	156 Na^+	0
Ca-0	78 Ca^{2+}	0
Na-0.5	156 Na^+	0.5 M NaCl
Ca-0.5	78 Ca^{2+}	0.5 M $CaCl_2$
Ca-0.3	78 Ca^{2+}	0.3 M $CaCl_2$
Ca-0.1	78 Ca^{2+}	0.1 M $CaCl_2$
Ca-0.05	78 Ca^{2+}	0.05 M $CaCl_2$

2.2 Simulation details

The force field parameters for Mt and APAM have been developed and validated in our previous work[29]. Briefly, the molecular topology of APAM was created by submitting its molecular structure to the GlycoBioChem PRODRG server[30]. Because PRODRG is compatible with GROMOS96 53A6 force field[31], the parameters for intra- and inter-molecular potentials were automatically generated. To confirm the accuracy of the partial atomic charges, geometrical optimization was performed using density functional theory (DFT) at B3LYP/6-31+G (d) level in Gaussian 16[32], followed by charge calculation using the CHelpG method[33]. Manual adjustment of partial atomic charges was then made to the topology file. More details on the topology of APAM were given in SI, section S1.1. SPC water model was adopted for the solvent and the ions were represented by GROMOS96 53A6 force field. Parameters for Mt were adopted from the CLAYFF force field[34,35] with all partial atomic charges unaltered.

The MD simulations were carried out in the GROMACS package[36–38] under NPT ensemble (isotropic pressure coupling) for 80 ns. Due to the application of periodic boundary conditions, the atoms in the simulation box were effectively moving between two charged Mt surfaces: plane

I in Figure 1b and plane II in the periodic image above. Therefore, unless otherwise specified any reference to Mt surface hereafter includes the consideration of both planes I and II. Before the NPT run, each system was minimized by the steepest descent method so as to limit the maximum force to 1000.0 kJ/(mol·nm), followed by equilibration in NVT ensemble for 100 ps. Nose-Hoover thermostat[39,40] and Parrinello–Rahman barostat[41] were employed to control the temperature and pressure at 300 K and 1 bar respectively. Equations of motions were integrated using the Leap-frog algorithm[42], with a time step of 1 fs. Constraints were applied to all the bonds using the LINC algorithm[43], except those in water which were constrained using the SETTLE algorithm. Cut-off distances for van der Waals and electrostatic interactions were both set to be 1.0 nm. PME method was used to calculate the long-range electrostatic interactions[44].

3. Results and Discussion

3.1 Effect of cation valence on APAM adsorption

Systems Na-0, Na-0.5, Ca-0, Ca-0.5 in the first set of simulations were used to study the role of valence in the adsorption of APAM on Mt. Snapshots of the final configurations for these systems are shown in the Supporting Information (SI), section S1.2. The density profiles (number per unit volume) of carbonyl oxygens (CO) near the Mt surface are shown in Figure 2a, plotted against Z coordinate, defined as the vertical distance measured upwards from the basal plane I of Mt (see Figure 1b). The profiles of other key atoms of APAM (amide N and carboxylate oxygen COO^-) are showed in SI, section S1.3, which correlated well with the density profile of CO.

Examination of the minimum distance between CO atoms and Mt surface demonstrated that CO became adsorbed at $Z \leq 0.43$ nm from the Mt surface (refer to SI, section S2.4 for more discussion on this criterion). Consider first the cases of monovalent ions, systems Na-0 and Na-0.5. The number density of CO remained ~0 when $Z < 0.5$ nm. The result shows that when there were no extra salts added and the aqueous environment contained only neutralizing monovalent ions (Na^+), it was difficult for the anionic polymer to approach Mt. In system Na-0.5 where 0.5 M NaCl was added besides the neutralizing Na^+, density of CO remained higher than that in system Na-0 near the Mt surface ($Z < 3.8$ nm). However, the values were still ~0 for $Z \leq 0.43$ nm, suggesting that it was still difficult for the polymer molecules to form stable adsorption on the surface in system Na-0.5.

Ions distributions, in terms of number density, near the Mt-water interface are shown in Figure 2b. The plot against full range of Z (Z = 0-10 nm) is shown in SI, section S1.3. Because of the periodic boundary condition, increase in Z corresponds to departure from plane I and approach to plane II in the periodic image above. Since planes I and II have the same surface properties, the distributions were found to be symmetric about Z = 4.7 nm (thickness of the Mt model was ~0.6 nm), and the number densities were constant between Z = 3.7 and 5.7 nm representing the bulk solution (see Figure S3). Thus, in Figure 2b, only the results for Z < 3 nm are shown.

The formation of electric double layer (EDL) was observed from the density profiles of counterions and co-ions[45]. Taking system Na-0.5 as an example, Na^+ displayed a pronounced peak at Z = 0.4 nm where the density of Cl^- was still 0. The region with Z = 0-0.4 nm can therefore be identified as the "stern layer" according to the EDL theory[46]. After Z = 0.4 nm, the density of co-ions (Cl^-) began to grow while the density of counterions (Na^+) decreased until both converged to the bulk value at Z = 1.39 nm (refer to SI section S2.1 for more details). The region where Z = 0.4-1.39 nm can be identified as the "diffuse layer". Stern layer and diffuse layer were divided by the outer Helmholtz plane (OHP), which corresponded to Z = 0.4 nm in this case. The outer location of the diffuse layer, 1.39 nm here, is a measure of the thickness of the EDL, at which the surface charge of Mt became neutralized (the cumulative charges for each system are shown in SI, section S1.4). The locations for the OHP and outer boundary of the EDL are marked in Figure 2b for all the systems. As shown in the figure, the thickness of the EDL in system Na-0.5 (1.39 nm) was smaller than that in system Na-0 (2.49 nm), consistent with the prediction from the Poisson-Boltzmann (PB) theory where the "decay length" reduces as salinity is increased.

In contrast to systems Na-0 and Na-0.5 where stable adsorption was absent, adsorption was observed when the neutralizing ions were replaced by Ca^{2+}, even without adding extra salts. As shown in Figure 2a, in system Ca-0, CO atoms started accumulating before Z = 0.43 nm, indicating that they became adsorbed. In Figure 2b the counterions (Ca^{2+}) converged to the bulk density at Z = 1.90 nm in system Ca-0, faster than the counterions in system Na-0. Similarly, ion densities in system Ca-0.5 converged to their bulk values at a shorter distance (Z = 1.35 nm) than that in system Na-0.5. To conclude, the EDL was suppressed by replacing monovalent ions with divalent ions ($Na^+ \rightarrow Ca^{2+}$); meanwhile adsorption of CO atoms on the surface was observed.

The number of adsorbed CO atoms was calculated by integrating the density profile in Figure 2a from both Mt surfaces to the distance of 0.43 nm from them. The results are summarized in Table 2, along with the thickness of EDL determined from Figure 2b and the Debye length predicted by PB theory. The number of adsorbed CO atoms followed the order of Na-0 = Na-0.5 < Ca-0.5 < Ca-0. The thickness of the EDL and the predicted Debye length followed the same sequence of Na-0 > Ca-0 > Na-0.5 > Ca-0.5. Interestingly, significantly enhanced adsorption was observed from Na-0.5 to Ca-0 evidenced by the much larger amounts of adsorbed CO in Ca-0, while the thickness of EDL was larger in system Ca-0. In addition, less adsorption was found in Ca-0.5 than in Ca-0 although the EDL was ~57% thinner in Ca-0.5. It can thus be inferred that besides suppressing the EDL, divalent Ca^{2+} played other roles in the adsorption of APAM on Mt.

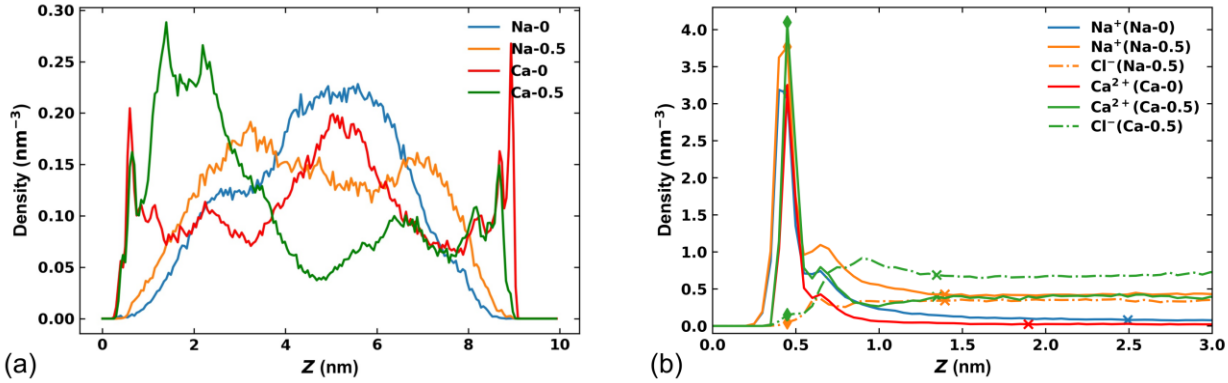

Figure 2 (a) Density profiles of carbonyl oxygens along *Z* axis, averaged over the last 20 ns of the simulations. (b) Density profile of counterions ions and co-ions along the *Z* axis, averaged over the last 20 ns of the simulations. For each system, the location of OHP is marked with diamond symbol, and the location where the EDL ends is marked with '×' symbol.

Table 2 Summary of number of adsorbed CO atoms per unit volume, EDL thickness, and decay length predicted by PB theory

system	No. adsorbed CO atoms in last 20 ns	thickness of EDL [a] (nm)	Debye length [b] (nm)
Na-0	0.02	2.49	0.73
Na-0.5	0.02	1.39	0.37
Ca-0	2.16	1.90	0.51
Ca-0.5	0.37	1.35	0.22

a. The calculation of EDL thickness for all systems are shown in SI, section S2.1. b. Predicted by PB theory, a measure of the EDL thickness. The Debye length κ^{-1} was calculated from $\kappa^{-1} = \left(\varepsilon_0 \varepsilon k_B T / \sum C_i e^2 z_i^2\right)^{1/2}$, where ε_0 is the permittivity of vacuum, ε is dielectric constant (78.4 for water), k_B is the Boltzmann constant, T is the temperature (300 K), C_i is the number density of i^{th} ion, z_i is the valence of i^{th} ions, and e is the elementary charge. The number of counterions (Na^+/Ca^{2+}) and co-ions (Cl^-) in each system are shown in SI, section S2.2.

3.2 Coordination to divalent ions

To further probe the role of Ca^{2+}, radial distribution functions (RDFs) of APAM carbonyl oxygen (CO), carboxylate oxygen (COO^-), and water oxygen (Ow) around Ca^{2+} in system Ca-0.5 are shown in Figure 3a. The first peak in the RDF of water was at ~0.25 nm (see enlarged inset in Figure 3a), indicating the solvation of Ca^{2+} ions[47]. Meanwhile, the first peak in the RDF of carbonyl oxygen was located at ~0.24 nm, suggesting that APAM formed a stable complex around Ca^{2+} at a distance similar to water.

To better understand the interactions of water and APAM with Ca^{2+}, system Ca-0.5 was examined in more detail by tracking two representative Ca^{2+} ions in the EDL, marked as Ca^{2+}_1 and Ca^{2+}_2. Based on 2000 snapshots uniformly sampled from the last 20 ns of the simulation, the number of water oxygens within 0.25 nm of Ca^{2+}_1, denoted by *N*, was calculated and plotted in Figure 3b (left panel, green segments) as a function of time. The histogram for *N* is shown in the same figure (right panel, green bars). As shown in the histogram, *N* was nearly normally distributed, and 92% of the data were in the interval of *N* = 4-7. Besides, all the atoms within 0.25 nm of Ca^{2+}_1 were found to be water oxygens after analyzing the atom types (refer to SI, section S2.3 for calculation details). This indicates the formation of a hydration shell around Ca^{2+}_1 by 4-7 water oxygens at the distance of 0.25 nm. Ca^{2+} ions and water oxygens are known to form coordinate covalent bonds[48]. The center Ca^{2+} and the surrounding water oxygens constituted a coordination complex. The coordinate bond length (0.25 nm) suggested by the first

peak in the RDF of water around Ca^{2+}, as well as the number of water oxygens per Ca^{2+} in the first coordination shell (4-7), are in good agreement with previous reports[48].

While the atoms within 0.25 nm of Ca^{2+}_1 were entirely water oxygens, atoms within 0.25 nm of Ca^{2+}_2 included two types, water oxygens and APAM CO. *N* vs. time for Ca^{2+}_2 is shown as red dots in the left panel of Figure 3b and the corresponding histogram is shown in the right panel as red bars. Here, 93% of the data fell into the range of 3-6, suggesting that Ca^{2+}_2 was coordinated to 3-6 water oxygens for most of the time. This range was lower than the number of water oxygens coordinated to Ca^{2+}_1. The '×' symbol in Figure 3b (left panel) represents the number of CO within 0.25 nm of Ca^{2+}_2, which fluctuated between 1-2. It can thus be deduced that in the first coordination shell of Ca^{2+}_2, 1-2 water oxygens were displaced by CO, while the same number of total oxygens were maintained as in the first coordination shell of Ca^{2+}_1. The close proximity between CO and Ca^{2+}_2 led to the formation of a Ca^{2+}-APAM complex.

While CO formed stable complex with Ca^{2+}, the number of COO^- oxygens that coordinated to Ca^{2+} was collected in SI, section S1.6. Table S2 showed that the binding of COO^- to Ca^{2+} was much less prominent than CO, which was also consistent with the weaker peak intensity of the COO^- RDF around Ca^{2+} shown in Figure 3a. The number of CO that coordinated to Na^+ is also shown in Table S2, where the binding of CO to Na^+ was much less favored compared with Ca^{2+}, suggesting that the replacement of water by APAM in the first coordination shell of Na^+ was much weaker."

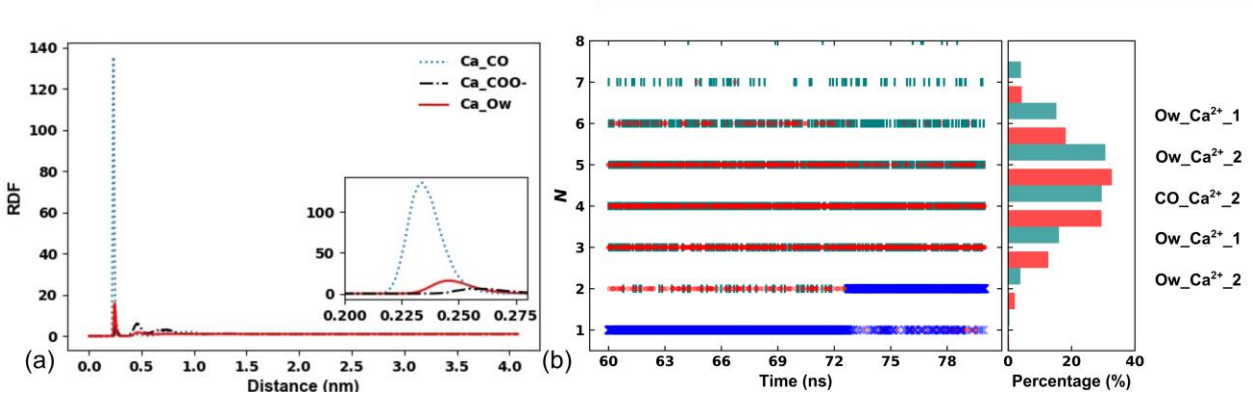

Figure 3 (a) RDFs of carbonyl oxygens of APAM (Ca_CO), carboxyl oxygens of APAM (Ca_COO^-), and water oxygens (Ca_Ow) around Ca^{2+} in system Ca-0.5. (b) Number (*N*) of water oxygens within 0.25 nm of Ca^{2+}_1 (left panel, green segments, one data every 1 ps) and statistical histograms for *N* (right panel, green bars). Corresponding data for Ca^{2+}_2 is shown as red dots for *N* vs. time and red bars in the histogram. Blue '×' in the left panel represents the carbonyl oxygens of APAM within 0.25 nm of Ca^{2+}_2. All data points were sampled from the last 20 ns simulation of system Ca-0.5.

To explore whether the coordination of APAM to Ca^{2+} was related to its adsorption on Mt, a three-dimensional (3-D) map was created to show the locations of adsorbed APAM CO that were simultaneously coordinated to at least one Ca^{2+} ions. Such a map is shown in Figure 4a for system Ca-0.5, based on data from the last 20 ns of the simulation (corresponding maps for systems Ca-0, 0.05, 0.1, 0.3 are given in SI, Section S1.4). To generate this map, a Ca^{2+} ion and a CO atom were said to be coordinated if this CO atom was within 0.24 nm of the Ca^{2+} ion (location of first peak in the RDF of CO around Ca^{2+} in Figure 3a), suggesting the formation of a Ca^{2+}-APAM complex. All CO atoms that were both adsorbed (refer to SI, section S2.4 for more discussion on this criterion) to Mt and coordinated to Ca^{2+}, i.e., those adsorbed from Ca^{2+}-APAM complexes, were mapped onto Figure 4a, with their *X*, *Y* coordinates as defined in Figure 1b, as well as their distance *D* to the nearest Mt surface (plane I or the periodic image of plane II). The Ca^{2+} ions in those adsorbed Ca^{2+}-APAM complexes were also mapped onto Figure 4a in the same way.

In Figure 4a, the Ca^{2+} ions stayed at an average distance of 0.42 nm from Mt, around the OHP (see Figure 2b). The CO atoms were located at a closer distance (average around 0.35 nm) within the stern layer of Mt. Therefore, unlike what was hypothesized in some literature[49], the Ca^{2+} ions did not serve as bridges sandwiched between APAM and Mt. Instead, our results showed that the Ca^{2+}-APAM complexes, which resulted from the coordination of carbonyl groups to solvated Ca^{2+}, carried residual positive charges and were subsequently attracted to Mt. Figure 4b shows an image of a Ca^{2+}-APAM complex near the OHP of the Mt surface. As shown in the enlarged area, there were five water oxygens and one APAM CO in the first coordination shell of the Ca^{2+} ion; the CO and Ca^{2+} were at similar distances from Mt in this image. The ability of Ca^{2+} to form a coordination complex with APAM and the lack of such ability by Na^{+} was the main reason for the significant improvement in adsorption from the Na^{+} systems to the Ca^{2+} systems as seen in Table 2.

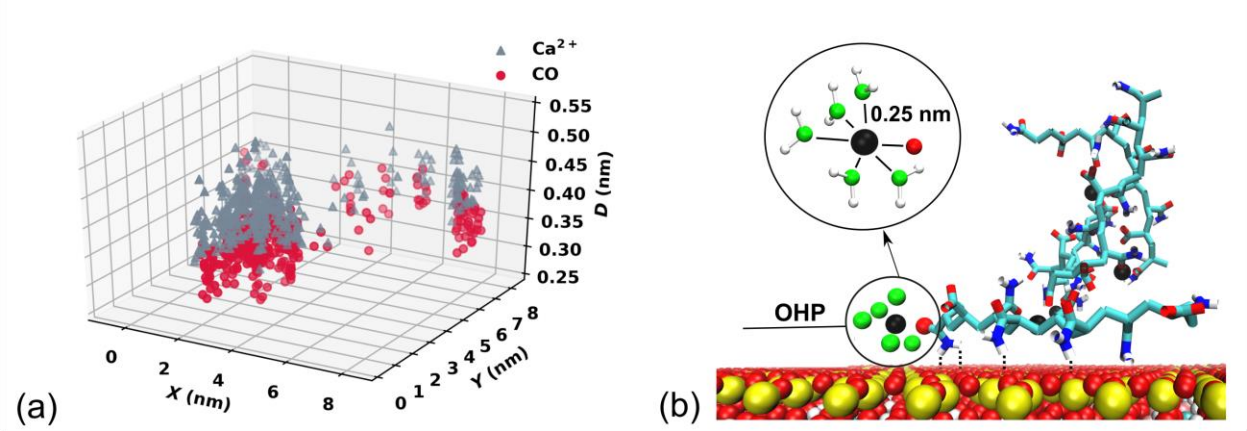

Figure 4 (a) 3-D map of CO and Ca^{2+} in Ca^{2+}-APAM complexes adsorbed on Mt, data from the last 20 ns of the simulation for system Ca-0.5. (b) Snapshot extracted from system Ca-0.1 at 65 ns. Green spheres represent water oxygen, while the other atoms are in the same color scheme as in Figure 1b.

3.3 Non-monotonic influence of salinity on the adsorption of Ca^{2+}-APAM complexes

One interesting observation from Table 2 was that APAM adsorption appeared to be reduced as the concentration of $CaCl_2$ increased from 0 to 0.5 M. To further investigate the effect of salinity, additional simulations were performed with $CaCl_2$ concentrations of 0.05 M, 0.1 M and 0.3 M. Snapshots of final configurations of these systems are shown in SI, section S1.1. Figure 5a shows the average number of Ca^{2+}-APAM complexes adsorbed on the Mt surface (N_{cpl}). N_{cpl} was determined in the same way as described in section 3.2, by counting the number of adsorbed APAM CO that were simultaneously coordinated to at least one Ca^{2+} ions. N_{cpl} was ~0.9 in system Ca-0, where the number of Ca^{2+} was just enough to neutralize the system. When the concentrations of $CaCl_2$ increased to 0.05 M and 0.1 M, N_{cpl} increased to 1 and 2, respectively. However, the increasing trend of N_{cpl} reversed when the concentration of $CaCl_2$ reached 0.3 M (N_{cpl} = 0.6) and continued decreasing to N_{cpl} = 0.2 at $CaCl_2$ concentration of 0.5 M, both lower than the value in system Ca-0.

To understand the non-monotonic trend of N_{cpl} with salinity, the cumulative charges around Mt were calculated and displayed in Figure 5b (results for full range of Z are given in SI, section S1.3). In system Ca-0, because of the distribution of counterions and APAM molecules in the EDL, the Mt surface charge was gradually compensated until the cumulative charge approached zero in the bulk solution. However, when additional $CaCl_2$ was added, the PB theory failed and the charge of Mt was overcompensated. This phenomenon can be attributed to the "ion-

correlation" effect, in which ions are no longer treated as point charges but have finite volume. It was shown that when electrostatic correlation was considered among ions with finite volume, free energy minimization of the system would lead to a surface charge reversal, and the "ion-correlation" effect was more prominent for multivalent ions than monovalent ions[50–52].

The average number of Ca^{2+} ions coordinated to each APAM molecule (including both adsorbed and unadsorbed ones) is plotted in the inset of Figure 5b (calculation details are in SI, section S2.5). As shown in Figure 4a, for the adsorbed Ca^{2+}-APAM complexes, the Ca^{2+} and CO were mostly within or around the OHP (Z = 0.4 nm) of Mt. In system Ca-0, the cumulative charge was negative around the OHP. The average number of Ca^{2+} coordinated to each APAM molecule was ~0.83, less than the Ca^{2+} needed to neutralize each APAM molecule (1.5 since each APAM carried a charge of -3). As a result, on average the electrostatic interaction between Ca^{2+}-APAM complexes and Mt was repulsive, which hindered their adsorption. In system Ca-0.05, the cumulative charge was also negative at OHP and became close to 0 after Z = 0.65 nm. The average number of Ca^{2+} coordinated to each APAM was around 1.33, indicating that the Ca^{2+}-APAM complexes were close to charge neutrality and their repulsion with Mt diminished. The cumulative charge around Mt in system Ca-0.1 was similar to that in Ca-0.05, negative at OHP and close to neutral after Z = 0.65 nm. The average number of Ca^{2+} coordinated to APAM was 1.65, thus the Ca^{2+}-APAM complexes carried a residual positive charge and were attracted by the long-range electrostatic interaction to the OHP. However, when the ion concentration further increased, i.e., represented by systems Ca-0.3 and Ca-0.5, the cumulative charge around Mt was positive after the OHP. Meanwhile, the average numbers of Ca^{2+} coordinated to each APAM were more than 1.5, resulting in residual positive charges. Hence there was a long-range electrostatic repulsion between the Ca^{2+}-APAM complexes and the OHP preventing the accumulation of the complexes in the EDL. To conclude, the adsorption of Ca^{2+}-APAM complexes on Mt surface had a non-monotonic dependence on Ca^{2+} concentration because the concentration regulated both the charge of the Ca^{2+}-APAM complexes and the cumulative charge near Mt surfaces, determining the long-range electrostatic interaction between them.

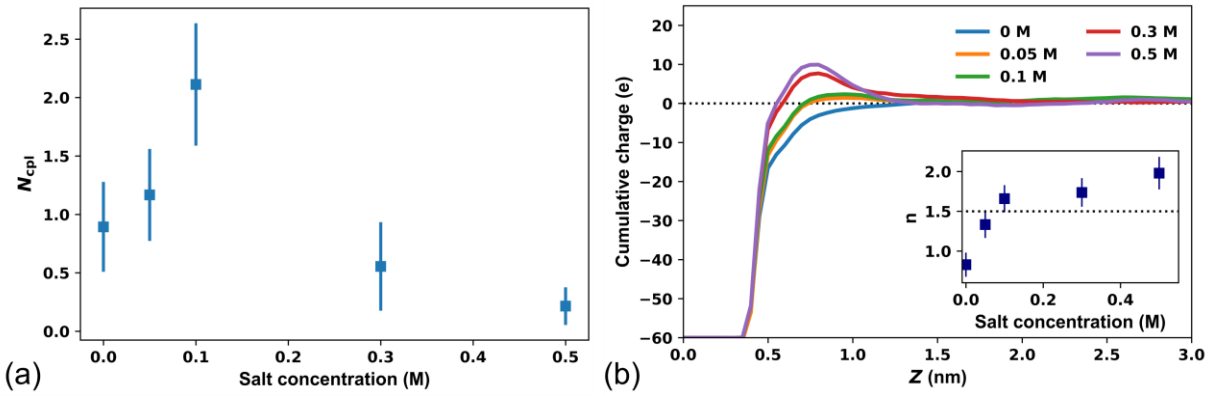

Figure 5 (a) Number of Ca^{2+}-APAM complexes adsorbed on Mt surfaces in systems Ca-0, 0.05, 0.1, 0.3 and 0.5. (b) Cumulative charges of Mt, APAM and ions in systems Ca-0, 0.05, 0.1, 0.3 and 0.5, as a function of *Z* coordinate. Average number (*n*) of Ca^{2+} coordinated to each APAM molecule is shown as inset. In (a) and inset of (b), error bar represents the standard deviation of data, which were collected from the last 20 ns of the simulation.

3.4 APAM adsorption through H-bonding facilitated by Ca^{2+} coordination

While the Ca^{2+} and CO of adsorbed Ca^{2+}-APAM complexes were located, on average, at a distance of 0.35-0.42 nm from Mt (see Figure 4a), the minimum distance between adsorbed APAM molecules and Mt was within 0.23 nm (see SI, section S2.4). This shorter distance suggests that other atom groups were forming closer contact with Mt. Analysis of the APAM atoms within 0.23 nm of Mt showed that all of them were hydrogens in the amino groups, which formed direct H-bonding with the surface oxygen of Mt. Hence, while the coordination of Ca^{2+} with APAM and the formation of Ca^{2+}-APAM complexes facilitated the long-range electrostatic attraction and the approach of the complexes to Mt, the short-range H-bonding stabilized the adsorption on the surface. The advantage of this synergy was that there was no competition of active sites on APAM between Ca^{2+} coordination and H-bonding. As illustrated in Figure 4b, H-bonds were formed through the amino groups in the amides of APAM, with H atoms pointing towards the oxygens of Mt, while Ca^{2+}-APAM complexes were formed through the carbonyl oxygens in the amides.

To quantify the synergetic effect above, the number of adsorbed APAM molecule is shown in Figure 6 as a function of time. Also shown are the percentage of CO in the adsorbed APAM that contributed to the formation of adsorbed Ca^{2+}-APAM complexes, as well as the percentage of amino hydrogens in the adsorbed APAM that contributed to H-bonding with Mt (more

calculation details in SI, section S2.6). These three quantities changed with time in synchronous manner and were highly correlated, confirming the synergy between Ca^{2+} coordination and H-bonding in APAM adsorption.

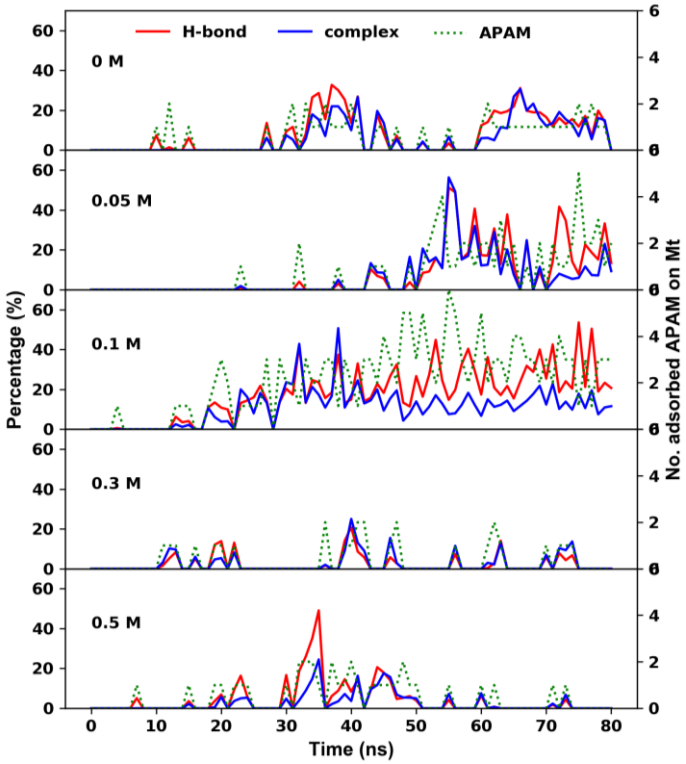

Figure 6 Percentage of CO in adsorbed APAM that contributed to the formation of adsorbed Ca^{2+}-APAM complexes (blue solid curve, left axis), percentage of amino hydrogen in adsorbed APAM that contributed to H-bonding with Mt (red solid curve, left axis), and number of adsorbed APAM molecules on Mt (green dashed line, right axis), in systems Ca-0, 0.05, 0.1, 0.3, and 0.5 respectively. Each point is an average of 100 sample points within the previous 1 ns.

In Figure 6, the number of adsorbed APAM molecules in all systems was less than 12, the total number of APAM in the simulation box. This result indicates that a fraction of the APAM molecules stayed in the bulk solution without being adsorbed on Mt. Analysis of these unadsorbed APAM revealed that Ca^{2+}-APAM complexes still formed (see SI, section 1.5 for details), affecting the cumulative charge around APAM. In addition, for the adsorbed APAM, the contribution from the Ca^{2+}-APAM complexes within could be significant. For example, when 0.05 M $CaCl_2$ was added, as high as 56% (at 56 ns) of the CO in the adsorbed APAM molecules was adsorbed on Mt in the form of complexes, stabilizing the polymer adsorption. It is worth mentioning that APAM could adsorb on Mt either as monomers or in the form of clusters. H-

bonding as well as Ca^{2+} coordination between different APAM molecules both contributed to the clustering. Detailed illustration of APAM-APAM interaction can be found in SI, section S1.8.

3.5 Discussion

Several mechanisms have been proposed in the literature for polymer adsorption mediated by divalent ions. Some argued that the charges of the solid and polymers were suppressed by the ions due to the screening effect[13], or even reversed due to ion correlation[18,19]. Some proposed that counterions became adsorbed on the polymers and/or solid through coordination and water displacing, and that the solid and polymers were bridged in the configurations of polymer-cation-solid[17] or polymer-water-cation-solid[14].

As revealed by the atomistic results in this work, when divalent ions were present, APAM tended to bind to Ca^{2+} by displacing 1-2 water in the first coordination shell of Ca^{2+}, forming Ca^{2+}-APAM complexes. The displacement of water was supported by the experimental study of Ait-Akbour et al.[17] in which water loss was reported upon the adsorption of anionic PCP on Mt interlayer. In addition, our results showed when the Ca^{2+}-APAM complex was attracted to the Mt surface, Ca^{2+} ions were located slightly further from Mt than the carbonyl oxygens of APAM, instead of forming a bridging structure in the form of APAM-Ca^{2+}-Mt or APAM-water-Ca^{2+}-Mt. Meanwhile, direct H-bonds were formed between the amino groups of APAM and surface oxygens of Mt, and there was a strong positive correlation between the degree of coordination, the number of H-bonds and the amount of APAM adsorption.

This work presented several new discoveries that differed from previous reports. Braganca et al.[16] attributed Ca^{2+}-enhanced anionic styrene-acrylic adsorption on Mt to “ion bridging” where Ca^{2+} ions were suggested to be located between Mt and styrene-acrylic. Deng et al.[14] proposed that the adsorption of APAM on smectite could be promoted through water bridges, where H-bonds were formed between APAM and water in the solvation shell of Ca^{2+}. Such bridging structures, in the form of APAM-Ca^{2+}-Mt or APAM-water-Ca^{2+}-Mt, were not observed in our simulations. Peng et al.[9] reported that Ca^{2+} could suppress H-bonding between APAM and kaolinite due to the competition of active sites, while our results showed the promotion of H-bonding by Ca^{2+}. In fact, our results demonstrated a new adsorption mechanism where different active sites on the APAM interact with different entities to cooperatively enhance the adsorption. The carbonyl oxygens were coordinated to Ca^{2+} while the nearby amino groups were H-bonded to Mt (see Figure 4b). This arrangement was able to simultaneously promote Ca^{2+}-APAM

interaction and APAM-Mt interaction. The cooperative interactions enabled by the different active sites of APAM also removed the requirement of an explicit "bridge" (Ca^{2+} or water) for the adsorption, as the amino groups were brought sufficiently close to Mt to establish the short-range stabilizing H-bonds.

Compared with divalent ions (Ca^{2+}), monovalent ions (Na^{+}) had two disadvantages in promoting APAM adsorption on Mt. The first is the less screening of the electrostatic repulsion between APAM and Mt. More importantly, Na^{+} lacked the ability to form Na^{+}-APAM complexes through coordination (Table S2). The long-range electrostatic interaction driving the Ca^{2+}-APAM complexes towards the solid was therefore missing, making it difficult to establish stable short-ranged interactions such as H-bonding.

Because the long-range electrostatic interaction regulated the initial approach of the polymers towards the solid, the effect of divalent ions on adsorption was concentration dependent. Our work showed a non-monotonic trend between the number of adsorbed Ca^{2+}-APAM complexes and the salt concentration, which provides explanations for several conflicting reports on the effect of ion concentration[9,15]. Increasing the dosage of multi-valent salts may promote or impede the polymer adsorption, depending on both the charge of the Ca^{2+}-APAM complexes and cumulative charge near the solid surface, the latter may be reversed as a result of ion correlation.

Several limitations exist in this work. Ions distribution as well as polymer adsorption vary with surface properties of the solid[47,53–55]. In this work, basal surface of Mt was selected to represent the solid for polymer adsorption. However, other types of surfaces exist in practical applications which might lead to different adsorption behaviors. For example, Bourg et al.[56] showed that when atom substitution on the basal surface of mica (sharing similar structure to Mt) was on the tetrahedral sheet instead of the octahedral sheet in this work, the counterions were adsorbed by forming inner surface complexes and an inner Helmholtz plane (IHP) could be identified. Besides, hydroxyl groups also exist on many solid surfaces, such as basal/edge surface of kaolinite and edge surface of Mt, which can promote the formation of H-bonds.

Lastly, as in any MD simulations using classical force fields, the force field parameters can have some influence on intermolecular interactions. For instance, Moucka et al.[57] demonstrated that physical properties such as density and chemical potential of $CaCl_2$ could be well modeled by classical force field (transferable $CaCl_2$ force field for Ca^{2+}, Dang-Smith force field for Cl^{-} and SPC/E water model) at ambient conditions when the salt concentration was less than 1 mol

kg^{-1}, while the prediction was poor at elevated temperature and pressure and high concentrations. Here in this work, we used CLAYFF for Mt, SPC model for water, and GROMOS force field for APAM and ions. There were extensive evidences[58–60] for the good compatibility of the three force fields, including our own validation[29]. Our simulations were performed under ambient conditions and the highest salt concentration used was 0.47 mol kg^{-1}, which is well within the regime where faithful modeling of aqueous $CaCl_2$ solution is expected. Nevertheless, as an exercise, we tested a different force field namely OPLSAA[61] for the APAM molecule and ions. Results from the additional simulation (SI, section S1.7) showed that the preferential coordination of Ca^{2+} with CO, as compared with COO^-, still held but the preference was less prominent. This sensitivity to force field is not surprising since classical force fields require the atomic charges to be constant while charge transfer may play a role in ion-polymer coordination. Additional DFT calculations (SI, section S1.7) did not show clear evidence that one force field (GROMOS or OPLSAA) was superior to the other, and extensively testing other force fields is out of the scope of this work. The adsorption mechanism reported in this work did hold for both force fields that we tested, including the lack of Ca^{2+} bridges and synergy with H-bonding, but future studies may have a more in-depth look at the force field dependence.

4. Conclusions

The adsorption of anionic APAM on Mt in saline solutions was investigated by all-atoms MD simulations. Divalent ions (Ca^{2+}) showed a much better enhancement of the polymer adsorption than monovalent ions (Na^+). Besides the better charge screening ability, Ca^{2+} was coordinated to the carbonyl oxygens of APAM, resulting in the formation of Ca^{2+}-APAM complexes. The Ca^{2+}-APAM complexes were subsequently captured into the EDL of Mt, but without the need of Ca^{2+} bridges. While the long-range electrostatic attraction drove the approach of Ca^{2+}-APAM complexes to Mt, short-range H-bonding formed directly between APAM and Mt provided an important stabilizing mechanism for the adsorption. A strong positive correlation was found between the degree of coordination, the number of H-bonds and the amount of APAM adsorption. A delicate balance was discovered when varying the concentration of $CaCl_2$. The best adsorption performance required an optimal concentration that did not under-neutralize or over-neutralize the charges of Mt or APAM. This work is a unique contribution to the fundamental understanding of polymer adsorption promoted by multi-valent

ions. To our knowledge, it is the first atomistic-level study that examined the interplay of charge screening, ion-ion correlation, cation coordination and hydrogen bonding for the adsorption of anionic polymer on like-charged solid surface. The results demonstrated a new mechanism of synergetic adsorption and explained the long-standing debate on the effect of salinity. New insights gained through this work highlighted the value of using molecular simulations to study polymer adsorption at a resolution much finer than that in experiments. Besides contributing to fundamental understanding, the present work also shed light onto applications in soil remediation, pharmaceutical formulation, wastes consolidation, cosmetics design, hydrogel fabrication, and many others. Future work involving different surfaces can allow us to further address the effect of surface properties on polymer adsorption.

Supporting Information

S1. Additional data

S2. Calculation details

Acknowledgements

We acknowledge the computing resources and technical support from Western Canada Research Grid (WestGrid), and financial support from the Natural Science and Engineering Research Council (NSERC) of Canada.

References

(1) Llamas, S.; Guzmán, E.; Baghdadli, N.; Ortega, F.; Cazeneuve, C.; Rubio, R. G.; Luengo, G. S. Adsorption of Poly(Diallyldimethylammonium Chloride)—Sodium Methyl-Cocoyl-Taurate Complexes onto Solid Surfaces. *Colloids Surfaces A Physicochem. Eng. Asp.* **2016**, *505*, 150–157.

(2) Ji, J.; Xiong, H.; Zhu, Z.; Li, L.; Huang, Y.; Yu, X. Fabrication of Polypyrrole/Chitosan Nanocomposite Aerogel Monolith for Removal of Cr(VI). *J. Polym. Environ.* **2018**, *26*, 1979–1985.

(3) Kausar, A.; Iqbal, M.; Javed, A.; Aftab, K.; Nazli, Z. i. H.; Bhatti, H. N.; Nouren, S. Dyes Adsorption Using Clay and Modified Clay: A Review. *J. Mol. Liq.* **2018**, *256*, 395–407.

(4) Zvulunov, Y.; Ben-Barak-Zelas, Z.; Fishman, A.; Radian, A. A Self-Regenerating Clay-Polymer-Bacteria Composite for Formaldehyde Removal from Water. *Chem. Eng. J.* **2019**,

374, 1275–1285.

(5) Lu, H.; Wang, Y.; Li, L.; Kotsuchibashi, Y.; Narain, R.; Zeng, H. Temperature- and PH-Responsive Benzoboroxole-Based Polymers for Flocculation and Enhanced Dewatering of Fine Particle Suspensions. *ACS Appl. Mater. Interfaces* **2015**, *7*, 27176–27187.

(6) Law, S. L.; Kayes, J. B. Adsorption of Non-Ionic Water-Soluble Cellulose Polymers at the Solid-Water Interface and Their Effect on Suspension Stability. *Int. J. Pharm.* **1983**, *15*, 251–260.

(7) Xiao, H.; Liu, Z.; Wiseman, N. Synergetic Effect of Cationic Polymer Microparticles and Anionic Polymer on Fine Clay Flocculation. *J. Colloid Interface Sci.* **1999**, *216*, 409–417.

(8) Molatlhegi, O.; Alagha, L. Adsorption Characteristics of Chitosan Grafted Copolymer on Kaolin. *Appl. Clay Sci.* **2017**, *150*, 342–353.

(9) Peng, F. F.; Di, P. Effect of Multivalent Salts-Calcium and Aluminum on the Flocculation of Kaolin Suspension with Anionic Polyacrylamide. *J. Colloid Interface Sci.* **1994**, *164*, 229–237.

(10) Long, J.; Li, H.; Xu, Z.; Masliyah, J. H. Role of Colloidal Interactions in Oil Sand Tailings Treatment. *AIChE J.* **2006**, *52*, 371–383.

(11) Theng, B. K. G. *Formation and Properties of Clay-Polymer Complexes*; Elsevier Science: Amstersam, 2012.

(12) Kohay, H.; Bilkis, I. I.; Mishael, Y. G. Effect of Polycation Charge Density on Polymer Conformation at the Clay Surface and Consequently on Pharmaceutical Binding. *J. Colloid Interface Sci.* **2019**, *552*, 517–527.

(13) Ji, Y.; Lu, Q.; Liu, Q.; Zeng, H. Effect of Solution Salinity on Settling of Mineral Tailings by Polymer Flocculants. *Colloids Surfaces A Physicochem. Eng. Asp.* **2013**, *430*, 29–38.

(14) Deng, Y.; Dixon, J. B.; White, G. N.; Loeppert, R. H.; Juo, A. S. R. Bonding between Polyacrylamide and Smectite. *Colloids Surfaces A Physicochem. Eng. Asp.* **2006**, *281*, 82–91.

(15) Vermöhlen, K.; Lewandowski, H.; Narres, H. D.; Schwuger, M. J. Adsorption of Polyelectrolytes onto Oxides - The Influence of Ionic Strength, Molar Mass, and Ca^{2+} Ions. *Colloids Surfaces A Physicochem. Eng. Asp.* **2000**, *163*, 45–53.

(16) Bragança, F. D. C.; Valadares, L. F.; De Leite, C. A. P.; Galembeck, F. Counterion Effect on the Morphological and Mechanical Properties of Polymer-Clay Nanocomposites

Prepared in an Aqueous Medium. *Chem. Mater.* **2007**, *19*, 3334–3342.

(17) Ait-Akbour, R.; Boustingorry, P.; Leroux, F.; Leising, F.; Taviot-Guého, C. Adsorption of PolyCarboxylate Poly(Ethylene Glycol) (PCP) Esters on Montmorillonite (Mmt): Effect of Exchangeable Cations (Na^+, Mg^{2+} and Ca^{2+}) and PCP Molecular Structure. *J. Colloid Interface Sci.* **2015**, *437*, 227–234.

(18) Dos Santos, A. P.; Girotto, M.; Levin, Y. Simulations of Polyelectrolyte Adsorption to a Dielectric Like-Charged Surface. *J. Phys. Chem. B* **2016**, *120*, 10387–10393.

(19) Wang, L.; Liang, H.; Wu, J. Electrostatic Origins of Polyelectrolyte Adsorption: Theory and Monte Carlo Simulations. *J. Chem. Phys.* **2010**, *133* (4).

(20) Long, J.; Xu, Z.; Masliyah, J. H. Adhesion of Single Polyelectrolyte Molecules on Silica, Mica, and Bitumen Surfaces. *Langmuir* **2006**, *22*, 1652–1659.

(21) Lu, Q.; Yan, B.; Xie, L.; Huang, J.; Liu, Y.; Zeng, H. A Two-Step Flocculation Process on Oil Sands Tailings Treatment Using Oppositely Charged Polymer Flocculants. *Sci. Total Environ.* **2016**, *565*, 369–375.

(22) Fraenkel, G.; Franconi, C. Protonation of Amides. *J. Am. Chem. Soc.* **1960**, *82*, 4478–4483.

(23) Saracino, G. A. A.; Improta, R.; Barone, V. Absolute PKa Determination for Carboxylic Acids Using Density Functional Theory and the Polarizable Continuum Model. *Chem. Phys. Lett.* **2003**, *373*, 411–415.

(24) Allen, E. W. Process Water Treatment in Canada's Oil Sands Industry: I. Target Pollutants and Treatment Objectives. *J. Environ. Eng. Sci.* **2008**, *7* (2), 123–138.

(25) Silva, R. D.; Chaparro, T. D. C.; Monteiro, I. S.; Dugas, P. Y.; D'Agosto, F.; Lansalot, M.; Martins Dos Santos, A.; Bourgeat-Lami, E. Tailoring the Morphology of Polymer/Montmorillonite Hybrid Latexes by Surfactant-Free Emulsion Polymerization Mediated by Amphipathic MacroRAFT Agents. *Macromolecules* **2019**, *52*, 4979–4988.

(26) Kaddour, H.; Gerislioglu, S.; Dalai, P.; Miyoshi, T.; Wesdemiotis, C.; Sahai, N. Nonenzymatic RNA Oligomerization at the Mineral-Water Interface: An Insight into the Adsorption-Polymerization Relationship. *J. Phys. Chem. C* **2018**, *122*, 29386–29397.

(27) Zhang, B.; Shi, W.; Yu, S.; Zhu, Y.; Zhang, R.; Tay, J. H. Adsorption of Anion Polyacrylamide from Aqueous Solution by Polytetrafluoroethylene (PTFE) Membrane as an Adsorbent: Kinetic and Isotherm Studies. *J. Colloid Interface Sci.* **2019**, *544*, 303–311.

(28) Viani, A.; Gualtieri, A. F.; Artioli, G. The Nature of Disorder in Montmorillonite by Simulation of X-Ray Powder Patterns. *Am. Mineral.* **2002**, *87*, 966–975.

(29) Sun, W.; Zeng, H.; Tang, T. Synergetic Adsorption of Polymers on Montmorillonite: Insights from Molecular Dynamics Simulations. *Appl. Clay Sci.* **2020**, *193*, 105654.

(30) Schüttelkopf, A. W.; Van Aalten, D. M. F. PRODRG: A Tool for High-Throughput Crystallography of Protein-Ligand Complexes. *Acta Crystallogr. Sect. D Biol. Crystallogr.* **2004**, *60*, 1355–1363.

(31) Oostenbrink, C.; Villa, A.; Mark, A. E.; Van Gunsteren, W. F. A Biomolecular Force Field Based on the Free Enthalpy of Hydration and Solvation: The GROMOS Force-Field Parameter Sets 53A5 and 53A6. *J. Comput. Chem.* **2004**, *25*, 1656–1676.

(32) Frisch, M. J.; Trucks, G. W.; Schlegel, H. B.; Scuseria, G. E.; Robb, M. A.; Cheeseman, J. R.; Scalmani, G.; Barone, V.; Petersson, G. A.; Nakatsuji, H., et al. *Gaussian 16*, Revision B. 01. Gaussian, Inc.: Wallingford, CT, 2016.

(33) Breneman, C. M.; Wiberg, K. B. Determining Atom-Centered Monopoles from Molecular Electrostatic Potentials – the Need for High Sampling Density in Formamide Conformational-Analysis,. *J. Comp. Chem.* **1990**, *11*, 361–373.

(34) Cygan, R. T.; Liang, J. J.; Kalinichev, A. G. Molecular Models of Hydroxide, Oxyhydroxide, and Clay Phases and the Development of a General Force Field. *J. Phys. Chem. B* **2004**, *108*, 1255–1266.

(35) Pouvreau, M.; Greathouse, J. A.; Cygan, R. T.; Kalinichev, A. G. Structure of Hydrated Gibbsite and Brucite Edge Surfaces: DFT Results and Further Development of the ClayFF Classical Force Field with Metal-O-H Angle Bending Terms. *J. Phys. Chem. C* **2017**, *121*, 14757–14771.

(36) Abraham, M. J.; Murtola, T.; Schulz, R.; Páll, S.; Smith, J. C.; Hess, B.; Lindahl, E.; Abraham, M. J.; Murtola, T.; Schulz, R., et al. Gromacs: High Performance Molecular Simulations through Multi-Level Parallelism from Laptops to Supercomputers. *SoftwareX* **2015**, *1–2*, 19–25.

(37) Pronk, S.; Páll, S.; Schulz, R.; Larsson, P.; Bjelkmar, P.; Apostolov, R.; Shirts, M. R.; Smith, J. C.; Kasson, P. M.; Van Der Spoel, D., et al. GROMACS 4.5: A High-Throughput and Highly Parallel Open Source Molecular Simulation Toolkit. *Bioinformatics* **2013**, *29*, 845–854.

(38) Berendsen, H. J. C. J. C.; van der Spoel, D.; van Drunen, R. GROMACS: A Message-Passing Parallel Molecular Dynamics Implementation. *Comput. Phys. Commun.* **1995**, *91*, 43–56.

(39) Nosé, S. A Molecular Dynamics Method for Simulations in the Canonical Ensemble. *Mol. Phys.* **1984**, *52*, 255–268.

(40) Hoover, W. G. Canonical Dynamics: Equilibrium Phase-Space Distributions. *Phys. Rev. A* **1985**, *31*, 1695–1697.

(41) Parrinello, M.; Rahman, A. Polymorphic Transitions in Single Crystals: A New Molecular Dynamics Method. *J. Appl. Phys.* **1981**, *52*, 7182–7190.

(42) Hockney, R. W.; Goel, S. P.; Eastwood, J. W. Quiet High-Resolution Computer Models of a Plasma. *J. Comput. Phys.* **1974**, *14*, 148–158.

(43) Hess, B.; Bekker, H.; Berendsen, H. J. C.; Fraaije, J. G. E. M. LINCS: A Linear Constraint Solver for Molecular Simulations. *J. Comp. Chem* **1997**, *18*, 1463–1472.

(44) Darden, T.; York, D.; Pedersen, L. Particle Mesh Ewald: An N·log(N) Method for Ewald Sums in Large Systems. *J. Chem. Phys* **1993**, *98*, 10089–10092.

(45) Stern, O. Zur Theorie Der Elektrolytischen Doppelschicht. *Zeitschrift für Elektrochemie und Angew. Phys. Chemie* **1924**, *30*, 508–516.

(46) Israelachvili, J. N. *Intermolecular and Surface Forces*, third ed.; Academic: New York, 2011.

(47) Bourg, I. C.; Lee, S. S.; Fenter, P.; Tournassat, C. Stern Layer Structure and Energetics at Mica-Water Interfaces. *J. Phys. Chem. C* **2017**, *121*, 9402–9412.

(48) Katz, A. K.; Glusker, J. P.; Beebe, S. A.; Bock, C. W. Calcium Ion Coordination: A Comparison with That of Beryllium, Magnesium, and Zinc. *J. Am. Chem. Soc.* **1996**, *118*, 5752–5763.

(49) Aliste, M. P.; MacCallum, J. L.; Tieleman, D. P. Molecular Dynamics Simulations of Pentapeptides at Interfaces: Salt Bridge and Cation-π Interactions. *Biochemistry* **2003**, *42*, 8976–8987.

(50) Kjellander, R.; Marčelja, S. Inhomogeneous Coulomb Fluids with Image Interactions between Planar Surfaces. III. Distribution Functions. *J. Chem. Phys.* **1988**, *88*, 7138–7146.

(51) Kjellander, R. Ion-Ion Correlations Effective Charges in Electrolyte and Macroion Systems. *Berichte der Bunsengesellschaft/Physical Chem. Chem. Phys.* **1996**, *100*, 894–

904.

(52) Jellander, R.; Marčelja, S.; Quirk, J. P. Attractive Double-Layer Interactions between Calcium Clay Particles. *J. Colloid Interface Sci.* **1988**, *126*, 194–211.

(53) Undabeytia, T.; Nir, S.; Rytwo, G.; Serban, C.; Morillo, E.; Maqueda, C. Modeling Adsorption - Desorption Processes of CU on Edge and Planar Sites of Montmorillonite. *Environ. Sci. Technol.* **2002**, *36*, 2677–2683.

(54) Lammers, L. N.; Bourg, I. C.; Okumura, M.; Kolluri, K.; Sposito, G.; Machida, M. Molecular Dynamics Simulations of Cesium Adsorption on Illite Nanoparticles. *J. Colloid Interface Sci.* **2017**, *490*, 608–620.

(55) Zeitler, T. R.; Greathouse, J. A.; Cygan, R. T.; Fredrich, J. T.; Jerauld, G. R. Molecular Dynamics Simulation of Resin Adsorption at Kaolinite Edge Sites: Effect of Surface Deprotonation on Interfacial Structure. *J. Phys. Chem. C* **2017**, *121*, 22787–22796.

(56) Bourg, I. C.; Sposito, G. Molecular Dynamics Simulations of the Electrical Double Layer on Smectite Surfaces Contacting Concentrated Mixed Electrolyte (NaCl-$CaCl_2$) Solutions. *J. Colloid Interface Sci.* **2011**, *360*, 701–715.

(57) Moučka, F.; Kolafa, J.; Lísal, M.; Smith, W. R. Chemical Potentials of Alkaline Earth Metal Halide Aqueous Electrolytes and Solubility of Their Hydrates by Molecular Simulation: Application to $CaCl_2$, Antarcticite, and Sinjarite. *J. Chem. Phys.* **2018**, *148*, 222832.

(58) Chen, Y.; Xue, S.; Xia, Q.; Li, H.; Liu, Q.; Li, B. S.; Tang, B. Z. Surface Effect on the Self-Assembly of Nanofibers Revealed by in Situ AFM Imaging and Molecular Simulation. *J. Phys. Chem. C* **2019**, *123*, 9292–9297.

(59) Galicia-Andrés, E.; Petrov, D.; Gerzabek, M. H.; Oostenbrink, C.; Tunega, D. Polarization Effects in Simulations of Kaolinite-Water Interfaces. *Langmuir* **2019**, *35*, 15086–15099.

(60) Gladytz, A.; John, T.; Gladytz, T.; Hassert, R.; Pagel, M.; Risselada, H. J.; Naumov, S.; Beck-Sickinger, A. G.; Abel, B. Peptides@mica: From Affinity to Adhesion Mechanism. *Phys. Chem. Chem. Phys.* **2016**, *18*, 23516–23527.

(61) Jorgensen, W. L.; Tirado-rives, J. The OPLS Potential Functions for Proteins. Energy Minimizations for Crystals of Cyclic Peptides and Crambin. *J. Am. Chem. Soc.* **1988**, *110*, 1658-1666.

TOC Graphic